

Supplementary Information

Solar evaporation with solute replacement towards real-world applications

Zhenyuan Xu*, Jie Yu, He Shan, Jiebing Wang, Jintong Gao, Zhanyu Ye, Ruzhu Wang*

Engineering Research Center of Solar Power and Refrigeration (MOE), Institute of Refrigeration and Cryogenics, Shanghai Jiao Tong University, Shanghai 200240, China

*Corresponding author: rzwang@sjtu.edu.cn, xuzhy@sjtu.edu.cn

Supplementary Note S1. Analysis of heat localization v.s. capillary flow

(1) Heat localization

In solar evaporation, solar energy is converted into thermal energy for vaporization. High evaporation rate is equivalent to high energy efficiency, which is decided by the heat loss during the energy conversion:

$$m = \frac{\alpha q_{\text{solar}} - \varepsilon \sigma (T^4 - T_{\infty}^4) - h (T - T_{\infty}) - k (T - T_{\infty})/L_{\text{heat}}}{h_{\text{fg}}} \quad (\text{S1})$$

where, m , α , q_{solar} , ε , σ , h , k and h_{fg} represent the area-averaged evaporation rate, solar absorptivity, solar irradiation density, emissivity of evaporator, Stephen Boltzmann constant, convective heat transfer coefficient, equivalent thermal conductivity of evaporator and vaporization enthalpy of water, respectively. T , T_{∞} and L_{heat} represent the interface temperature, ambient/bulk solution temperature and transport distance from interface to bulk solution, respectively. The four parts on right side of the equation denote solar input, radiative heat loss, convective heat loss to air and heat loss to bulk solution, respectively. To achieve high evaporation rate, minimizing heat loss to bulk solution could be an effective way, through low thermal conductivity and longer transport pathway. This is also the choice of thermally-localized solar evaporation.

Parameter settings for radiative, conductive and convective heat transfer were as follows.

-The standard one-sun illumination was considered as the energy input. For simplification, the solar absorptivity and IR emissivity of the evaporator are set as 100%, by considering the evaporator as ideal black-body. This is close to the carbon based evaporator under wet state.

-The estimation of equivalent thermal conductivity for evaporator is complicated, due to the co-existence of convection and conduction inside porous evaporator. It will be affected by the flow rate, density, specific heat capacity, intrinsic thermal conductivity and porosity. Considering a highly porous evaporator with water inside and low flow rate of water, the equivalent thermal conductivity of evaporator is assumed to be same with that of water, i.e., $0.6 \text{ W m}^{-1} \text{ K}^{-1}$.

-A low level of natural convection is considered, and convective heat transfer coefficient of $5 \text{ W m}^{-2} \text{ K}^{-1}$ is used. Evaporator temperature and ambient temperature are considered as $30 \text{ }^\circ\text{C}$ and $20 \text{ }^\circ\text{C}$, respectively.

(2) Capillary flow

After the evaporation rate is confirmed, the mass flow rate from bulk water to air-liquid interface could be calculated. Based on the viscosity of fluid and permeability of porous media, the viscous loss of fluid flow through the porous evaporator could be obtained. Except for this, the upward raise of water will also induce the gravitational pressure change. To maintain the stable and continuous flow, capillary pressure generated by the porous media p_c needs to be higher than the sum of pressure drop Δp (calculated from Darcy's law) and gravitational pressure drop:

$$p_c \geq \Delta p + \rho g L_{\text{mass}} = \frac{m_{\text{sol}} L_{\text{mass}} \mu}{\rho k_p} + \rho g L_{\text{mass}} \quad (\text{S2})$$

$$m_{\text{sol}} = \frac{m}{1 - c_b} \quad (\text{S3})$$

where, ρ , g , c_b , μ and k_p represent the solution density, gravitational acceleration, bulk solution concentration, solution viscosity and permeability, respectively. Obviously, higher evaporation rate and longer transport pathway result in higher viscous pressure drop. To be mentioned, the mass flow rate of solution m_{sol} is slightly higher than the evaporation rate of water m , due to the existence of solute. The mass flow rate of solution is calculated from $m/(1-c_b)$, which is almost the same with evaporation rate for low-concentration bulk solution. The permeability of porous evaporator here is similar to that of porous carbon materials, which was set as 10^{-13} . The maximum capillary pressure generated by the porous media is considered equivalent to the gravitational pressure of water with 20 cm height (L_0), as shown in Eq. S4. This is in consistent with the experimental observations of many capillary wicking materials.

$$p_c = \rho g L_0 \quad (\text{S4})$$

To obtain the maximum evaporation rate $m_{\text{max, cap}}$ considering effective capillary pumping, the flow resistance caused by passive evaporation should be balanced with the capillary pressure generated by porous media:

$$p_c = \Delta p_{\max} + \rho g L_{\text{mass}} = \frac{m_{\max, \text{cap}}}{\rho(1 - c_b)} \frac{L_{\text{mass}} \mu}{k_p} + \rho g L_{\text{mass}} \quad (\text{S5})$$

Substitute Eq. (S4) into Eq. (S5), the maximum evaporation rate limited by capillary pumping (without the energy balance consideration) could be obtained as:

$$m_{\max, \text{cap}} = \rho^2 g \frac{k_p}{L_{\text{mass}} \mu} (1 - c_b) (L_0 - L_{\text{mass}}) \quad (\text{S6})$$

The maximum capillary height for salt solution $L_{\text{mass}, \text{max}}$ under a given evaporation rate m could then be calculated through Eq. S7.

$$L_{\text{mass}, \text{max}} = \frac{p_c}{\frac{m}{\rho(1 - c_b)} \frac{\mu}{k_p} + \rho g} \quad (\text{S7})$$

When the evaporator has longer heat loss and capillary pumping distances than $L_{\text{mass}, \text{max}}$, the capillary pumping is failed under the given evaporation rate, and dry-out of evaporator will occur.

(3) Different considerations in conventional and proposed design

In the above analysis, L_{mass} represents the capillary flow distance between the bulk solution and air-liquid interface, which is equivalent to the heat loss distance L_{heat} in conventional solar evaporator. In the proposed design, the salt rejection pathway is decoupled with the heat loss pathway, which ensures a much shorter capillary flow pathway of L_{mass} than the heat loss pathway of L_{heat} . To be precise, we also measured the thickness of FO-membrane used in this study (0.07 mm), which is adopted as the L_{mass} for the proposed design.

The same consideration of heat loss and salt rejection distances are also adopted for the later analysis of maximum evaporation rate under different solution solubility.

Supplementary Note S2. Analysis of heat localization vs. salt rejection.

When we analyze the conflict between heat localization and salt rejection, the consideration about heat localization is the same with that in Supplementary Note 1. As for the stable salt rejection, it is considered in two aspects including the salt accumulation flux and salt rejection flux shown below.

(1) Salt accumulation flux

The salt accumulation rate J_A refers to that at the air-liquid interface, which is caused by the evaporation of water from solution. It is calculated based on the evaporation rate and bulk solution concentration. Here, the bulk solution concentration was set as 3.5 wt%, considering a common level for NaCl solution for seawater simulation.

$$J_A = m \frac{c_b}{1 - c_b} \quad (\text{S8})$$

(2) Salt rejection flux

The salt rejection rate J_R is calculated from the diffusion of salt from interface to the bulk solution, with concentrations of c_i and c_b , respectively.

$$J_R = \frac{D (c_i - c_b)}{L_{\text{mass}}} \quad (\text{S9})$$

where, the mass transport distance L_{mass} is equal to the heat transfer distance and further decided by the thermal localization under a certain evaporation rate. The estimation for equivalent diffusion coefficient of solute D could be complicated, due to the same reason for equivalent thermal conductivity estimation. For simplification, it was set the same with the intrinsic diffusion coefficient of dissolved salt in water.

To achieve the steady state evaporation, salt accumulation flux should be equal to the salt rejection flux. To ensure no crystal deposition, the concentration at air-liquid interface should be lower than the maximum concentration without crystallization. In this case, the maximum salt rejection flux $J_{R,\text{max}}$ could be obtained, when the concentration at air-liquid interface is equal to the saturated solution concentration c_{sat} .

$$J_{R,\text{max}} = \frac{D (c_{\text{sat}} - c_b)}{L_{\text{mass}}} \quad (\text{S10})$$

(3) Maximum evaporation rate calculated from solubility

To avoid salt accumulation, the salt rejection flux should be higher than the salt accumulation flux, and the interfacial concentration should be lower than the saturated concentration. In another word, the maximum salt rejection flux should be higher than the salt accumulation flux, as shown below.

$$J_{R,\max} \geq J_A \quad (\text{S11})$$

The maximum evaporation rate could then be obtained, when the salt accumulation flux and maximum salt rejection flux are the same. By substituting Eqs. S8, S9 into Eq S11, the maximum evaporation rate limited by the salt rejection capability of saturated concentration (without the energy balance consideration) is:

$$m_{\max, \text{ saturated}} = \frac{D (c_{\text{sat}} - c_b) (1 - c_b)}{L_{\text{mass}} c_b} \quad (\text{S12})$$

Here, the saturation concentration c_{sat} could be calculated from the weight solubility S , thus evaluating the relation between maximum evaporation rate and solution solubility.

$$c_{\text{sat}} = \frac{S}{100+S} \quad (\text{S13})$$

With the above equations, the impacts of solution solubility on energy efficiency and maximum evaporator thickness could then be calculated.

Except for the pervious analysis, the saturated concentration required for a certain condition can also be evaluated, when the maximum salt rejection flux is equal to the salt accumulation flux under a certain evaporation rate. It could directly reflect the difference between the evaporation of high-solubility and low-solubility solutions. Based on Eq. S12, required saturated concentration can be calculated from:

$$c_{\text{sat}} = c_b + \frac{m L_{\text{mass}} c_b}{D(1 - c_b)} \quad (\text{S14})$$

Due to the increase of L_{heat} ($=L_{\text{mass}}$) under higher evaporation rate m , the required saturated concentration will increase rapidly with evaporation rate. This makes the salt precipitation extremely challenging, for the fast evaporation of low-solubility solution.

Except for the aforementioned equations and consideration, the analysis in Fig.1 in main text also adopts the following parameters, summarized in Table S1.

Table S1. Summary of the parameters for theoretical analysis [1-4].

Solar flux q_{solar}	1 kW m ⁻²	Ambient temperature T_{∞}	20°C
Latent heat of water evaporation h_{fg}	2400 kJ kg ⁻¹	Solar absorptivity α	100%
IR emissivity of evaporator ε	100%	Convective heat transfer coefficient h	5 W m ⁻² K ⁻¹
Equivalent thermal conductivity of evaporator k	0.6 W m ⁻¹ K ⁻¹	Density ρ	1000 kg m ⁻³
Steady-state capillary height L_0	20 cm	Permeability k_p	10 ⁻¹³

Supplementary Note S3. Analysis of maximum solar evaporation rates considering solution property

By combining the theoretical framework in Supplementary Notes S1-S2, the dominating mechanisms of solar evaporation can be captured, as shown in Fig. S1. (1) The three mechanisms supporting a stable solar evaporation including heat localization, capillary pumping and salt rejection. (2) The intertwined relationships between heat localization, capillary pumping and salt rejection, with the same water/evaporation flux m and transport distance (heat transport distance $L_{\text{heat}} =$ mass transport distance L_{mass}). (3) The relation between heat localization/capillary pumping/salt rejection and evaporator properties (including solar absorptivity α , equivalent thermal conductivity k , IR emissivity ε , pore size r , permeability k_p , evaporation height L), solution properties (including solution density ρ , surface tension σ_c , saturated concentration c_{sat} , viscosity μ , equivalent diffusion coefficient of solute D) and working conditions (solar flux q_{solar} , evaporation rate m , ambient temperature T_{∞} , bulk solution concentration c_{∞} and convective heat transfer coefficient h).

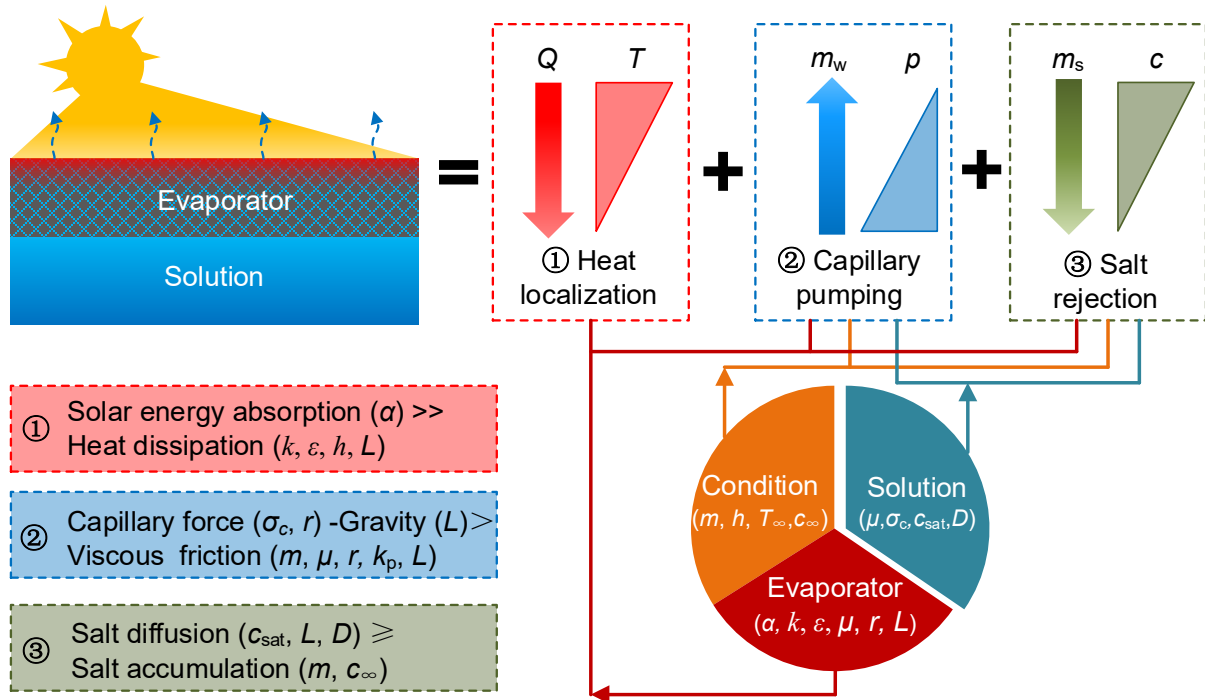


Fig. S1. The dominating mechanisms of solar evaporation captured by our proposed framework, including ①heat localization, ②capillary pumping and ③salt rejection. They

are intertwined and affected by evaporator properties, solution properties and working conditions.

With the theoretical framework, the maximum solar evaporation rates considering solution property can then be evaluated.

(1) Maximum evaporation rate considering effective capillary pumping

Considering the energy balance and capillary pumping, the minimum heat transport distance for heat localization $L_{\text{heat,min,1}}$ and the maximum solution transport distance for capillary pumping $L_{\text{mass,max,1}}$ can be calculated from evaporation rate as shown below.

$$L_{\text{heat, min,1}} = \frac{k(T - T_{\infty})}{\alpha q_{\text{solar}} - \varepsilon \sigma (T^4 - T_{\infty}^4) - h(T - T_{\infty}) - mh_{\text{fg}}} \quad (\text{S15})$$

$$L_{\text{mass, max,1}} = \frac{P_c}{\frac{m}{\rho(1 - c_b)} \frac{\mu}{k_p} + \rho g} \quad (\text{S16})$$

where, the parameter definitions could be found in our Supplementary Note 1. As shown in Eq. S15, the minimum evaporator height/transport distance will not change as long as the latent heat h_{fg} and working conditions keep constant. Different from this, the maximum evaporator height /transport distance is strongly affected by parameters including viscosity, as shown in Eq. S16. Due to the equivalent transport distance for heat and solution, the dry-out issue triggers when the minimum transport distance for heat localization $L_{\text{heat,min,1}}$ surpasses the maximum transport distance for capillary pumping $L_{\text{mass,max,1}}$. Maximum evaporation rates without dry-out issue can be obtained in Eq. S17, when $L_{\text{heat,min,1}}$ equals to $L_{\text{mass,max,1}}$.

$$m_{\text{max,1}} = \frac{\alpha q_{\text{solar}} - \varepsilon \sigma (T^4 - T_{\infty}^4) - h(T - T_{\infty}) - \frac{k(T - T_{\infty})}{P_c} \rho g}{\frac{k(T - T_{\infty})}{P_c} \frac{1}{\rho(1 - c_b)} \frac{\mu}{k_p} + h_{\text{fg}}} \quad (\text{S17})$$

For pure water with low viscosity, $L_{\text{heat,min,1}}$ increases rapidly with the evaporation rate while the $L_{\text{mass,max,1}}$ decreases very slow, showing a very high critical evaporation rate (Fig. S2). This also explains why capillary pumping is not the bottleneck in previous studies. However, the maximum capillary height decreases rapidly under high viscosity. When the

viscosity is 100 times or 1000 times higher, the capillary pumping failure occurs under evaporation rates of $1.17 \text{ kg m}^{-2} \text{ h}^{-1}$ and $0.66 \text{ kg m}^{-2} \text{ h}^{-1}$, respectively (Fig. S2).

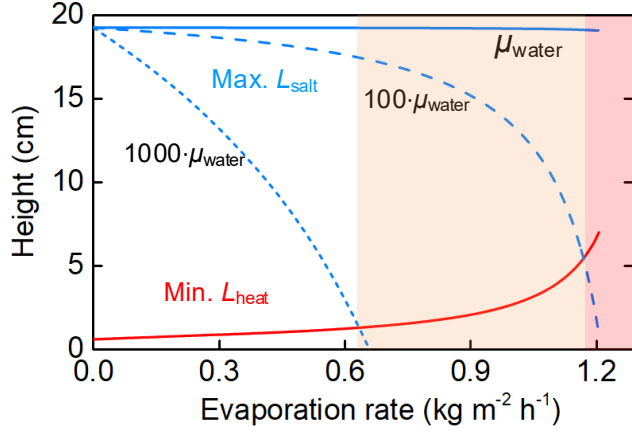


Fig. S2. Minimum evaporator height/transport distance for heat localization (red curve) and maximum capillary heights (blue curves) as functions of evaporation rate. Maximum capillary heights are calculated from different viscosities of μ_{water} (water viscosity), $100 \mu_{\text{water}}$ and $1000 \mu_{\text{water}}$. The pink and orange regions indicate the capillary pumping failure under $100 \mu_{\text{water}}$ and $1000 \mu_{\text{water}}$, respectively.

For solar evaporation with solute replacement, the heat localization and solution transport are decoupled, and the viscous losses of bulk solution transport are significantly reduced. Assuming the L_{heat} is R times longer than L_{mass} , the maximum evaporation rates without dry-out issue for solar evaporation with solute replacement can be obtained in Eq. S18.

$$m_{\max,1} = \frac{\alpha q_{\text{solar}} - \varepsilon \sigma (T^4 - T_{\infty}^4) - h (T - T_{\infty}) - \frac{k \rho g (T - T_{\infty})}{R p_c}}{h_{\text{fg}} + \frac{k (T - T_{\infty})}{\rho (1 - c_b)} \frac{\mu}{R \cdot p_c k_p}} \quad (\text{S18})$$

When the ratio R is approaching infinite, the impact of capillary pumping on maximum evaporation rate diminishes as shown in Eq. S19, which is decided by only energy balance. This indicates that the negative effect of capillary pumping could be eliminated, when the ratio R is large enough.

$$\lim_{R \rightarrow \infty} m_{\max,1} = \frac{\alpha q_{\text{solar}} - \varepsilon \sigma (T^4 - T_{\infty}^4) - h (T - T_{\infty})}{h_{\text{fg}}} \quad (\text{S19})$$

(2) Maximum evaporation rate considering effective salt rejection

Considering the energy balance and salt transport, the salt accumulation rate J_A and maximum salt rejection rate $J_{R,\max}$ are calculated under different transport distances.

$$J_A = \frac{\alpha q_{\text{solar}} - \varepsilon \sigma (T^4 - T_{\infty}^4) - h (T - T_{\infty}) - k (T - T_{\infty}) / L_{\text{heat}}}{h_{\text{fg}}} \frac{c_b}{1 - c_b} \quad (\text{S20})$$

$$J_{R,\max} = \frac{D (c_{\text{sat}} - c_b)}{L_{\text{mass}}} \quad (\text{S21})$$

where, the parameter definitions could be found in our Supplementary Note 1. The salt deposition issue triggers when the salt accumulation rate J_A is higher than the maximum salt rejection rate $J_{R,\max}$. Considering the ratio R equals to $L_{\text{heat}}/L_{\text{mass}}$, another maximum heat transport distance $L_{\text{heat,max,2}}$ limited by salt rejection can be obtained as shown in Eq. S22.

$$L_{\text{heat,max,2}} = R L_{\text{mass,max,2}} = \frac{R h_{\text{fg}} D \frac{(1 - c_b)(c_{\text{sat}} - c_b)}{c_b} + k (T - T_{\infty})}{\alpha q_{\text{solar}} - \varepsilon \sigma (T^4 - T_{\infty}^4) - h (T - T_{\infty})} \quad (\text{S22})$$

Substituting Eq. S22 into Eq. S1 in Supplementary Note 1, the maximum evaporation rate $m_{\max,2}$ limited by both energy balance and salt rejection can be obtained in Eq. S23.

$$m_{\max,2} = \frac{\alpha q_{\text{solar}} - \varepsilon \sigma (T^4 - T_{\infty}^4) - h (T - T_{\infty})}{h_{\text{fg}}} \left[1 - \frac{1}{\frac{R h_{\text{fg}} D (c_{\text{sat}} - c_b) (1 - c_b)}{k (T - T_{\infty}) c_b} + 1} \right] \quad (\text{S23})$$

For the conventional solar evaporation with $R = L_{\text{heat}}/L_{\text{mass}} = 1$, the salt accumulation rate increases and maximum salt rejection rate decreases under higher evaporation rate as shown in Fig. S3, resulting in a maximum evaporation rate of $1.12 \text{ kg m}^{-2} \text{ h}^{-1}$ for the analyzed scenario (Table S1, 3.5 wt% NaCl). Since the maximum salt rejection rate is calculated based on both the evaporation rate and saturated concentration, lower solubility will cause the degradation of maximum salt rejection rate. The required solubility to avoid

salt deposition is also higher under high evaporation rate (the purple curve in Fig. S3, calculated from Eq. S23).

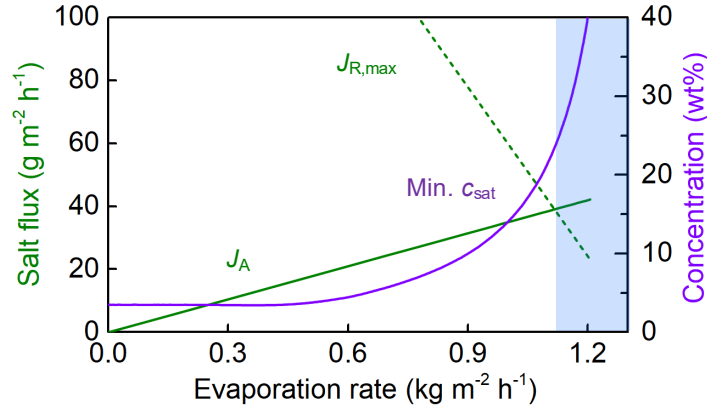


Fig. S3. The salt accumulation rate (cyan solid line), maximum salt rejection rate (cyan dashed line) of 3.5 wt% NaCl solution, and the minimum saturated concentrations ensuring no salt precipitation (purple curve) under different evaporation rates. The blue region represents the salt rejection failure.

For the solar evaporation with solute replacement with a larger ratio of R ($L_{\text{heat}}/L_{\text{mass}}$), the negative impact of salt rejection could be weakened. When the ratio R is approaching infinite, the maximum evaporation rate shown in Eq. S23 can be simplified to Eq. S24, which is decided by only energy balance and same with Eq. S19.

$$\lim_{R \rightarrow \infty} m_{\text{max},2} = \frac{\alpha q_{\text{solar}} - \varepsilon \sigma (T^4 - T_{\infty}^4) - h (T - T_{\infty})}{h_{\text{fg}}} \quad (\text{S24})$$

(3) Salt deposition issue for a mixed solution

In the real case of seawater desalination, the solution is typically mixed and contains multiple salts. In such scenario, the salt accumulation flux and rejection flux differ due to variations in the initial concentrations and solubility of distinct salts. Salts characterized by higher initial concentrations and lower solubility are more prone to salt deposition, thereby making the behavior of the most challenging salt species pivotal in mixed solutions.

Moreover, the final accumulation of salt is profoundly reliant on the diffusion coefficients of dissolved salts.

To quantitatively illustrate this matter, we calculated the salt accumulation rate and the maximum salt rejection rate under various evaporation rates for various salt species. As shown in Fig. S4, the salt accumulation rate of the calculated salt species escalates while the maximum salt rejection rate diminishes as the evaporation rates increase. Based on the concentration of salt ions in seawater and the order of crystallization during evaporation [5], NaCl, MgSO₄, and CaSO₄ in seawater are selected for analysis. Their concentrations are measured with seawater sample from Bohai Sea, and their saturated concentrations at ambient temperature are adopted. Besides, the salt diffusion coefficients are also collected from literatures [6-8]. All calculation parameters are shown in Table R1.

Table S2. Parameters for the different salts dissolved in seawater [5-8].

	Saturated concentration c_{sat} (wt%)	Concentration in seawater c_b (wt%)	Diffusion coefficient D (m ² s ⁻¹)
NaCl	26.5%	2.94%	1.99×10^{-9}
CaSO ₄	0.254%	0.116%	7.90×10^{-10}
MgSO ₄	25.2%	0.237%	7.50×10^{-10}

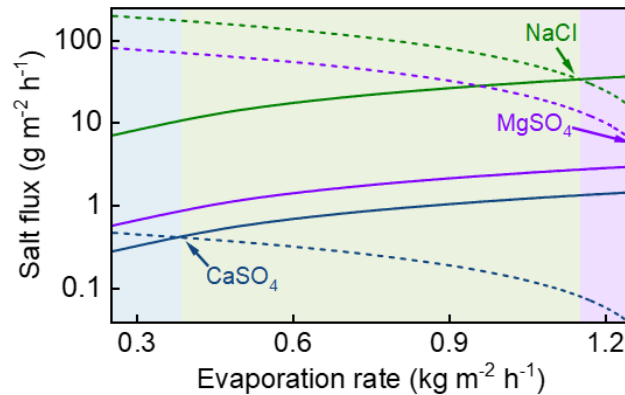


Fig. S4. Analysis of solar evaporation of the mixed solution. The salt accumulation rate (solid line), maximum salt rejection rate (dashed line) of the different salt species (NaCl, MgSO₄, and CaSO₄ in seawater) under different evaporation rates. The crossing between

salt accumulation rate curve and salt rejection curve indicates the critical condition for salt deposition. The three regions from left to right represent the acceptable evaporation rates for CaSO_4 , NaCl , and MgSO_4 , respectively.

The critical evaporation rate without salt deposition can be ascertained when these two salt transport rates become equivalent. In the examined scenario, the respective values for NaCl , MgSO_4 , and CaSO_4 amount to $1.15 \text{ kg m}^{-2} \text{ h}^{-1}$ (slightly higher than that in Fig. S3 due to lower NaCl concentration here), $1.25 \text{ kg m}^{-2} \text{ h}^{-1}$, and only $0.37 \text{ kg m}^{-2} \text{ h}^{-1}$. This further shows the effectiveness of our proposed framework in analyzing the complicated and practical issues.

Supplementary Note S4. Comparison of the solution properties.

To find the proper working fluid of solar evaporation device with solute replacement, several types of solution were selected and compared, including the NaCl, MgCl₂, NH₄HCO₃^[9], LiCl and [C₃H₄O₂]_n (poly acrylic acid, PAA) solutions. These choices are either commonly used draw solution in forward osmosis desalination, or working fluid for solar driving atmosphere water harvesting. The solubility, viscosity, osmotic pressure, hygroscopicity and volatility were compared as follows.

(1) Solubility: high solubility is preferred.

This is an intrinsic property of solution, so we summarized the solubility of these solutions under ambient temperature in Table S2. The solubility of NaCl, MgCl₂, NH₄HCO₃ and LiCl could be easily compared, with different units. However, solubility of PAA varies with different molecular weights, typically ranging from 2000 to 5000. In general, all the inorganic salts have much higher solubility than the organic PAA.

Table S2. Solubility of different salts under 20 °C.

	Solubility (g/100gH ₂ O)	Solubility (mol/100gH ₂ O)
NaCl	36	0.615
MgCl ₂	54.6	0.575
LiCl	67	1.58
NH ₄ HCO ₃	21.6	0.275
PAA	<2	Depending on the molecular weight of PAA [2000-5000]

(2) Viscosity: low viscosity is preferred.

Viscosity is related to the molecular size, so inorganic solute with smaller molecular size have lower viscosity. As shown in Table S3, NaCl, MgCl₂, NH₄HCO₃, LiCl solution all have low viscosity. They have quite similar viscosities under same weight concentration. For the viscosity under same molar concentration, LiCl solution exhibits slightly higher viscosity, due to the lower molecular weight. As for the PAA with large molecular size, its aqueous solution viscosity is much higher.

Table S3. Viscosity of different salts at 25 °C.

	Concentration	Viscosity (mPa·s)
NaCl	10 wt%	1.08
	1 mol/L	1.0
MgCl ₂	10 wt%	1.26
	1 mol/L	1.24
LiCl	10 wt%	3.2
	1 mol/L	1.6
NH ₄ HCO ₃	1-10 mol/L	1.2-2.5
PAA	1 wt%	>600

(3) Osmotic pressure: high osmotic pressure is preferred.

As the osmotic pressure is proportional to the ion number contained in the solution, the saturated molar concentration and ion number per molecule will decide the maximum osmotic pressure generated by the solution. Among the five choices, each MgCl₂ molecule could release three ions, each NaCl/LiCl molecule could release two ions, each NH₄HCO₃ molecule could release less than two ions, and PAA can only exist in the form of molecule.

Table S4. Osmotic pressure that various solutions can generate under saturation state or with the mass fraction of 100 g L⁻¹

	Concentration	Osmotic pressure (atm)
NaCl	100 g L ⁻¹	83.7
	Saturation	248
MgCl ₂	100 g L ⁻¹	77.1
	Saturation	335
NH ₄ HCO ₃	100 g L ⁻¹	115.4
	Saturation	109
LiCl	100 g L ⁻¹	55.7
	Saturation	588
PAA	Saturation	< 2

As shown in Table S4, the osmotic pressure of five choices can be evaluated under two different conditions, including the osmotic pressure under same mass concentration and

maximum osmotic pressure under saturated condition. (1) For the osmotic pressure under same mass concentration, this is decided by the ion numbers per molecule and the molecular weight. Higher molecular weight means less molecule numbers under the same weight concentration. Since the molecular weight of NaCl, MgCl₂, LiCl and NH₄HCO₃ are 58, 95, 42 and 79 respectively, the osmotic pressure under same weight concentration could be ranked as follows: LiCl > MgCl₂ ≈ NaCl > NH₄HCO₃ >> PAA. (2) Together with the saturated concentration, the maximum osmotic pressure of these solutions can be calculated and ranked as follows: LiCl > MgCl₂ > NaCl > NH₄HCO₃ >> PAA.

(4) Hygroscopicity: weak hygroscopicity is preferred.

Hygroscopicity describes the affinity between water vapor and the solution, which will reduce the water vapor pressure and increase the evaporation temperature. In this case, weak hygroscopicity is preferred. In general, the NaCl, NH₄HCO₃ and PAA exhibits almost no hygroscopicity, while the LiCl and MgCl₂ have hygroscopicity. Table S5 shows the water vapor pressure of NaCl, LiCl and MgCl₂ solution under different concentrations from 10 wt% to 25 wt%. The vapor pressure under low concentration are quite similar, but differs under high concentration. The vapor pressure of MgCl₂ solution is slightly lower than that of NaCl solution, while the LiCl solution exhibits much lower vapor pressure. This indicates the weak and strong hygroscopicity of MgCl₂ solution and LiCl solution, respectively. This is also in consistent with the common application of LiCl in dehumidification or atmosphere water harvesting, where strong hygroscopicity is necessary. Considering NH₄HCO₃ is decomposable and PAA has very low solubility, their water vapor pressures are not provided.

Table S5. Vapor pressure of different solutions.

	Concentration	Vapor pressure (mmHg)
NaCl	10 wt%	30
	20 wt%	27
	25 wt%	25
MgCl ₂	10 wt%	29
	20 wt%	25

	25 wt%	21
LiCl	10 wt%	29
	20 wt%	23
	30 wt%	15.5
NH ₄ HCO ₃	/	NA(decomposable)
PAA	/	NA(very low solubility)

(5) Volatility: non-volatility of solute is preferred.

The stable solute is necessary in the open solar evaporation system, so volatility of solute should be avoided. Except that the NH₄HCO₃ will decompose under low temperature, all other choices include NaCl, MgCl₂, LiCl and PAA are quite stable.

(6) Property comparison

Fig. S5 summarizes the property comparison of the five choices. The viscosity is evaluated under concentration of 10wt%, which is closer to the common working conditions. The water vapor pressure is evaluated under concentration of 25 wt%, since the difference of hygroscopicity matters under higher concentration. The maximum osmotic pressure is evaluated under their own saturated concentrations. Considering the very low solubility of PAA, its osmotic pressure and water vapor pressure are not provided. Considering the decomposition of NH₄HCO₃ solution, its water vapor pressure is not provided.

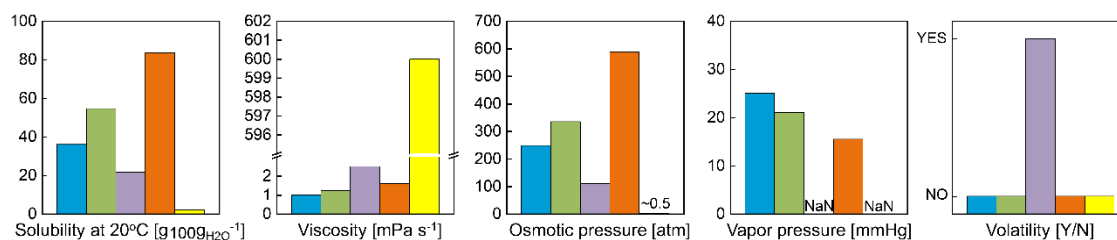


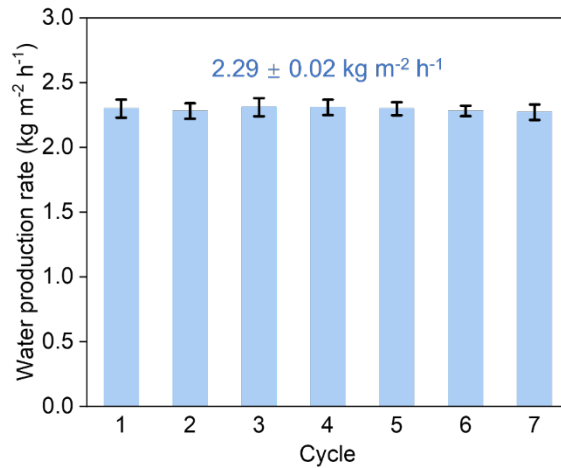
Fig. S5. A comprehensive quantitative analysis that conducted to assess the solubility, viscosity, osmotic pressure, hygroscopicity, and volatility characteristics of various solutions comprising NaCl, MgCl₂, NH₄HCO₃, LiCl and PAA (indicated with same colors as Fig. 2f). The primary objective of this study was to facilitate the selection of an

appropriate working fluid. Remarkably, the NaCl and MgCl₂ solutions demonstrated exceptional performance across all five aspects of interest, thereby highlighting their desirable properties.

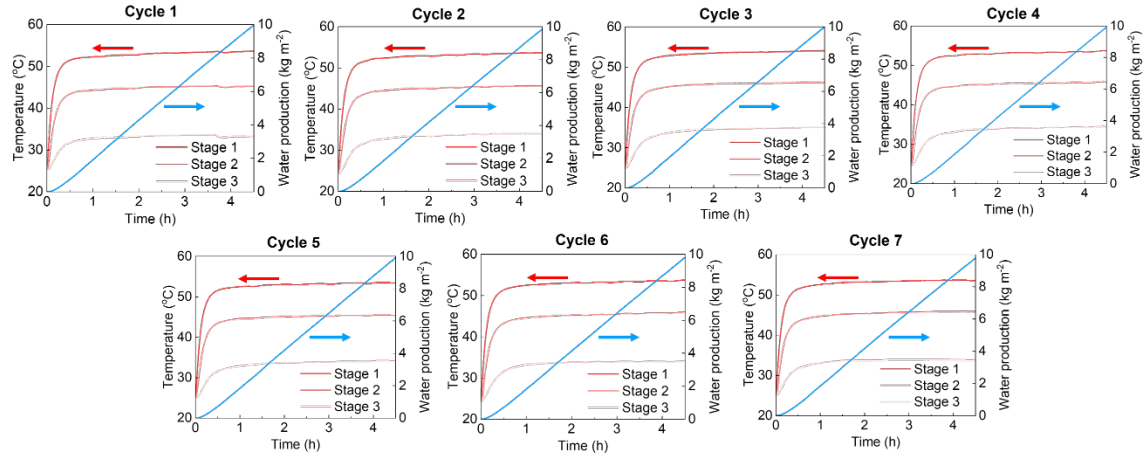
Supplementary Note S5. Long-term solar distillation test with solute replacement.

To demonstrate the long-term serviceability, we performed a continuous seven-day distillation experiment with the three-stage device to assess the stability of our system. Each cycle was conducted with a 4.5-h distillation process (Joule heating with 1 kW m^{-2}) followed by a 19.5-h passive rinsing process, to simulate the working conditions in real-world application. The solute replacement approach effectively mitigates salt deposition and contamination concerns, and the possible salt deposition on the evaporator can be removed effectively by the rinsing flow induced by siphonic effect.

Our test exhibited exemplary stability, showcasing average water production rates of $2.29 \pm 0.02 \text{ kg m}^{-2} \text{ h}^{-1}$ during the seven cycles (Fig. S6), and no discernible performance deterioration. The average water production rate here was calculated as the average value of the water production rates in the distillation process of 1.0 – 4.5 h for each cycle. The 4.5-h distillation test showed stable water productions of $9.78 - 10.01 \text{ kg m}^{-2}$ in each cycle, and the condenser temperatures after 4.5-h distillation were $53.34 - 54.10 \text{ }^\circ\text{C}$, $45.21 - 46.23 \text{ }^\circ\text{C}$, and $33.26 - 35.02 \text{ }^\circ\text{C}$ for the three distillation stages, respectively. The unwavering and satisfactory distillation performance observed throughout the 7-cycle investigation serves as compelling evidence of the resilience and dependable functionality of our system.



(a)



(b)

Fig. S6. Testing results of the seven-day solar distillation test with solute replacement. (a) Average water production rates of the three-stage device. The device showed average water production rates of $2.29 \pm 0.02 \text{ kg m}^{-2} \text{ h}^{-1}$ during the seven-day experiment. (b) Time lapse condenser temperatures and water productions of the seven-day test. The distillation test showed water productions of $9.78 - 10.01 \text{ kg m}^{-2}$ during the 4.5-h distillation process, and the condenser temperatures after 4.5-h distillation were $53.34 - 54.10 \text{ }^\circ\text{C}$, $45.21 - 46.23 \text{ }^\circ\text{C}$, and $33.26 - 35.02 \text{ }^\circ\text{C}$, respectively.

Supplementary Note S6. Economic analysis.

The three-stage solar distillation device with/without solute replacement was designed with commercially-available and low-cost materials. The three-stage solar distiller was fabricated with similar design in our previous research ^[10], so the material cost analysis is also similar. According to the fabrication shown in Method part and our previous experience, the retail cost of each part is summarized below.

Table S6. Summary for cost analysis ^[10,11]

Item	Unit cost	Cost	Component
AR glass	\$0.43/kg	\$0.01	Convection cover
Selective absorber	\$6.54/m ²	\$0.07	Solar absorber
Paper towel	\$0.21/m ²	\$0.03	Evaporator
Aluminum	\$2.03/kg	\$0.09	Condenser
Resin	\$4.5/kg	\$0.35	Distiller frame
Membrane	\$40/m ²	\$0.33	FO Membrane
Total without membrane	--	\$0.55	Conventional device
Total with membrane	--	\$0.88	Proposed device

It could be seen that the proposed device only has 1.6 times higher cost than the conventional device, while the lifetime of the device is increased not only 1.6 times. This indicates the effective reduction of water production cost. If more stage numbers and insulation with aerogel are adopted for higher efficiency, the cost difference between the solar distiller with/without solute replacement will be smaller.

Supplementary Figures S7-S22.

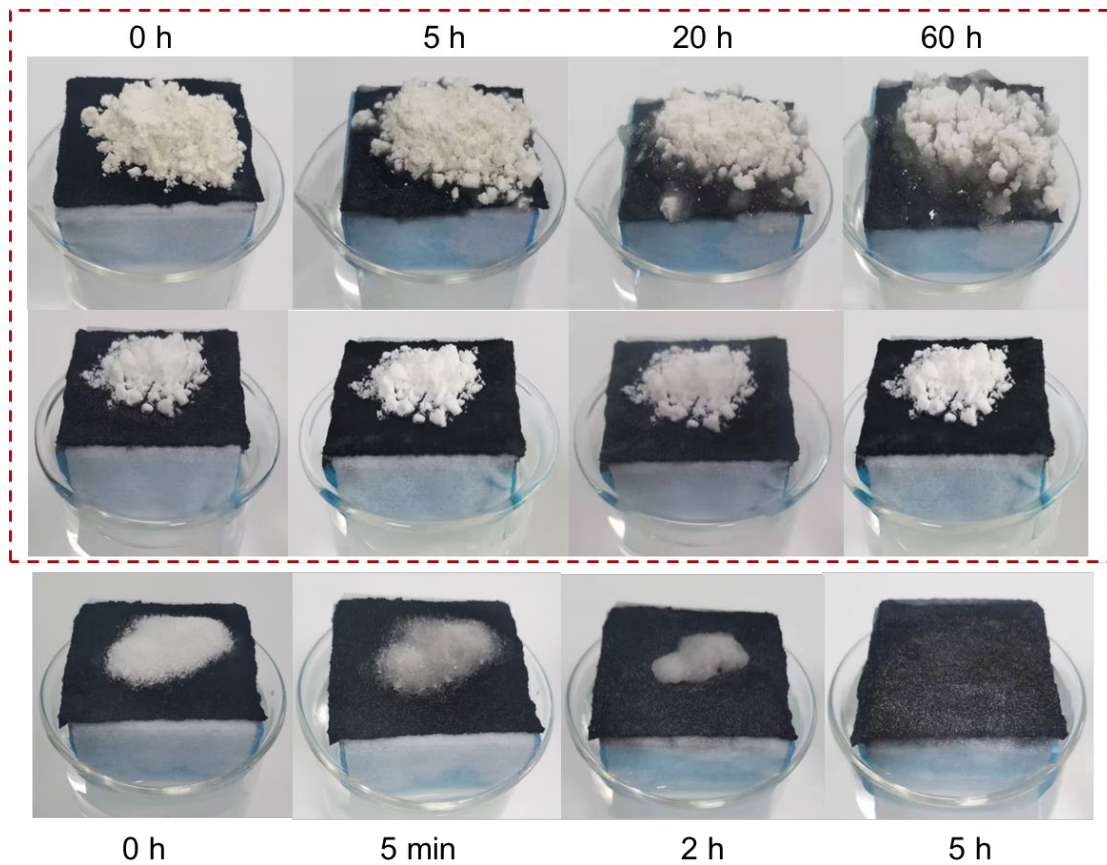


Fig. S7. Time-lapse salt rejection processes. Same amount of 1.0 g NaAlg, CaSO₄ and NaCl was deposited on the evaporator, as shown in the top, medium and bottom rows, respectively. Passive rejection processes of NaAlg and CaSO₄ were recorded for 60 hours, showing very little amount of dissolved salt. As for the passive rejection of NaCl, the majority of salt was dissolved within two hours, and all the salt was dissolved in five hours.

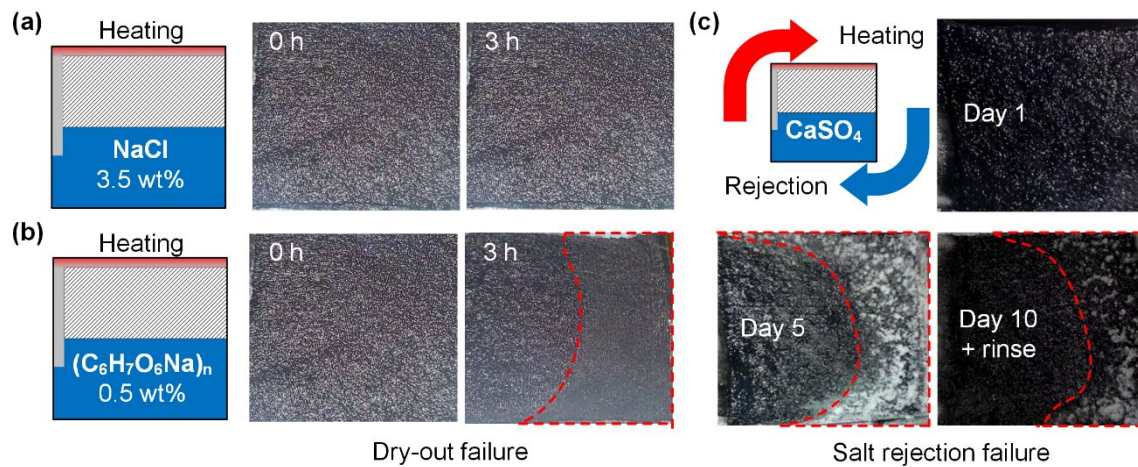
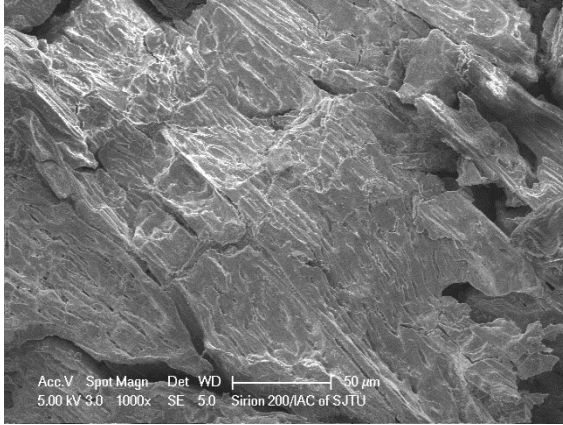
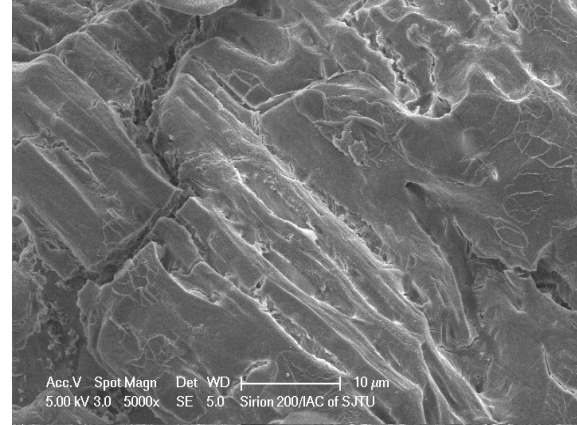


Fig. S8. Solar evaporation with different salt solution and the failure demonstration.

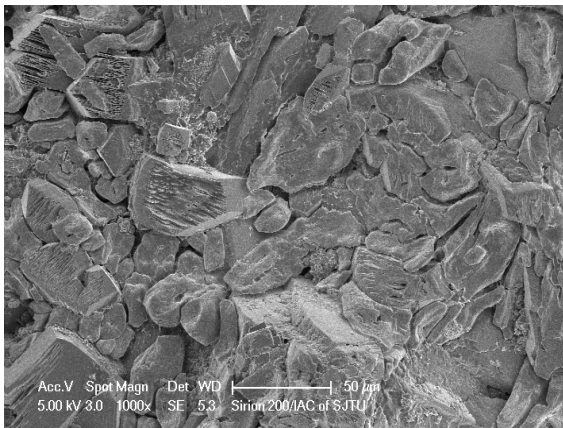
(a) Evaporation of 3.5 wt% NaCl solution. (b) Evaporation of 0.5 wt% NaAlg solution with high viscosity. Red curved region shows the dry-out region after 3-hour test. (c) Evaporation of $CaSO_4$ solution with low solubility. Red curved region shows the fouling region after 5-day test, which cannot be totally removed by rinse.



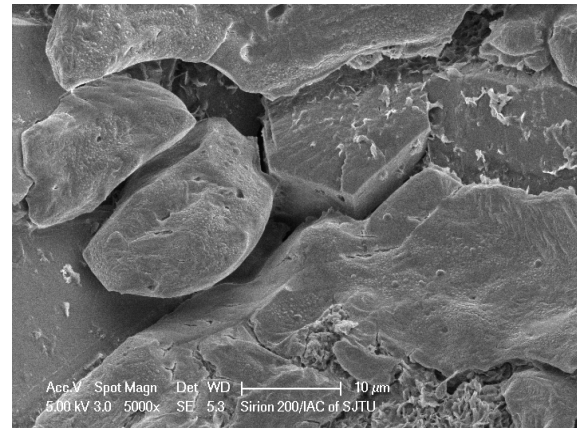
(a)



(b)



(c)



(d)

Fig. S9. SEM images of CaSO_4 fouling on solar evaporator. (a) (b) Top views of CaSO_4 crystals with different amplification ratios. (c) (d) Cutting views of CaSO_4 crystals with different amplification ratios. All the SEM images show compact crystal structures.

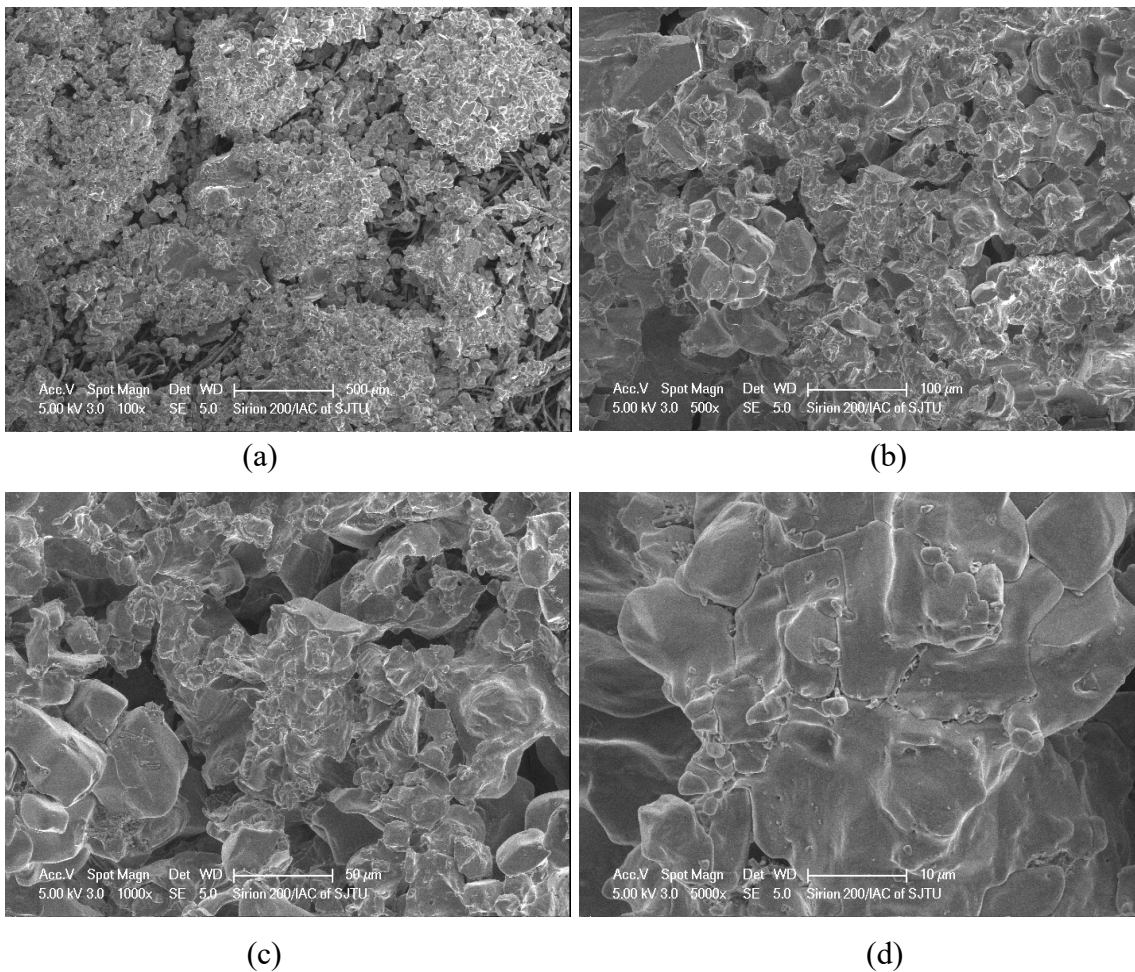


Fig. S10. SEM images of NaCl crystallization on solar evaporator. Different amplification ratios were adopted, with scale bars were 500 μm (a), 100 μm(b), 50 μm(c) and 10 μm(d). Random pores with 10-100 μm sizes could be observed.



Fig. S11. Solar evaporation device with solute replacement.

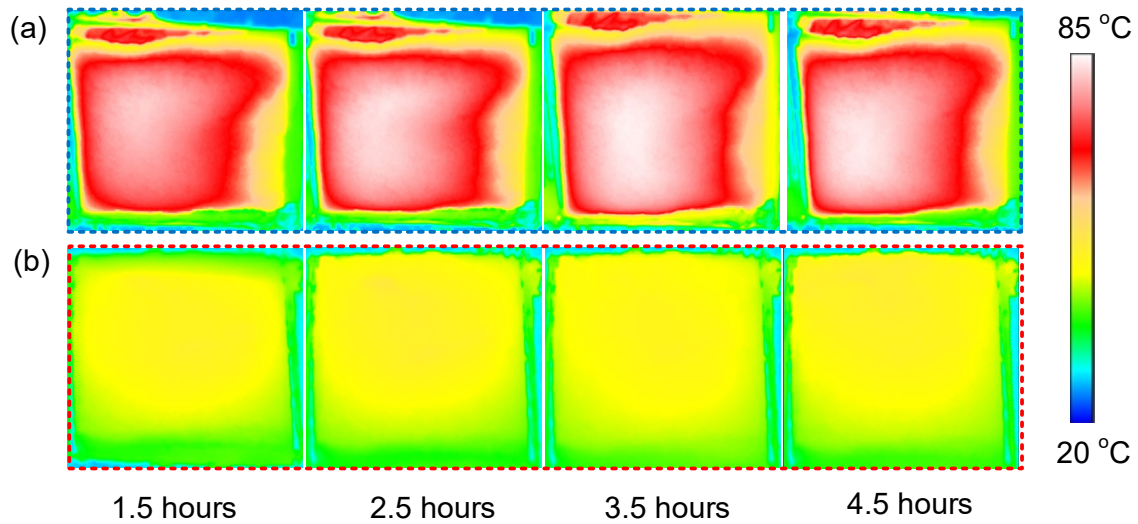


Fig. S12. Solar evaporation of the 1.0 wt% NaAlg solution with solute replacement and conventional designs. (a) IR images of the solar evaporation without solute replacement. (b) IR images of the solar evaporation with solute replacement.

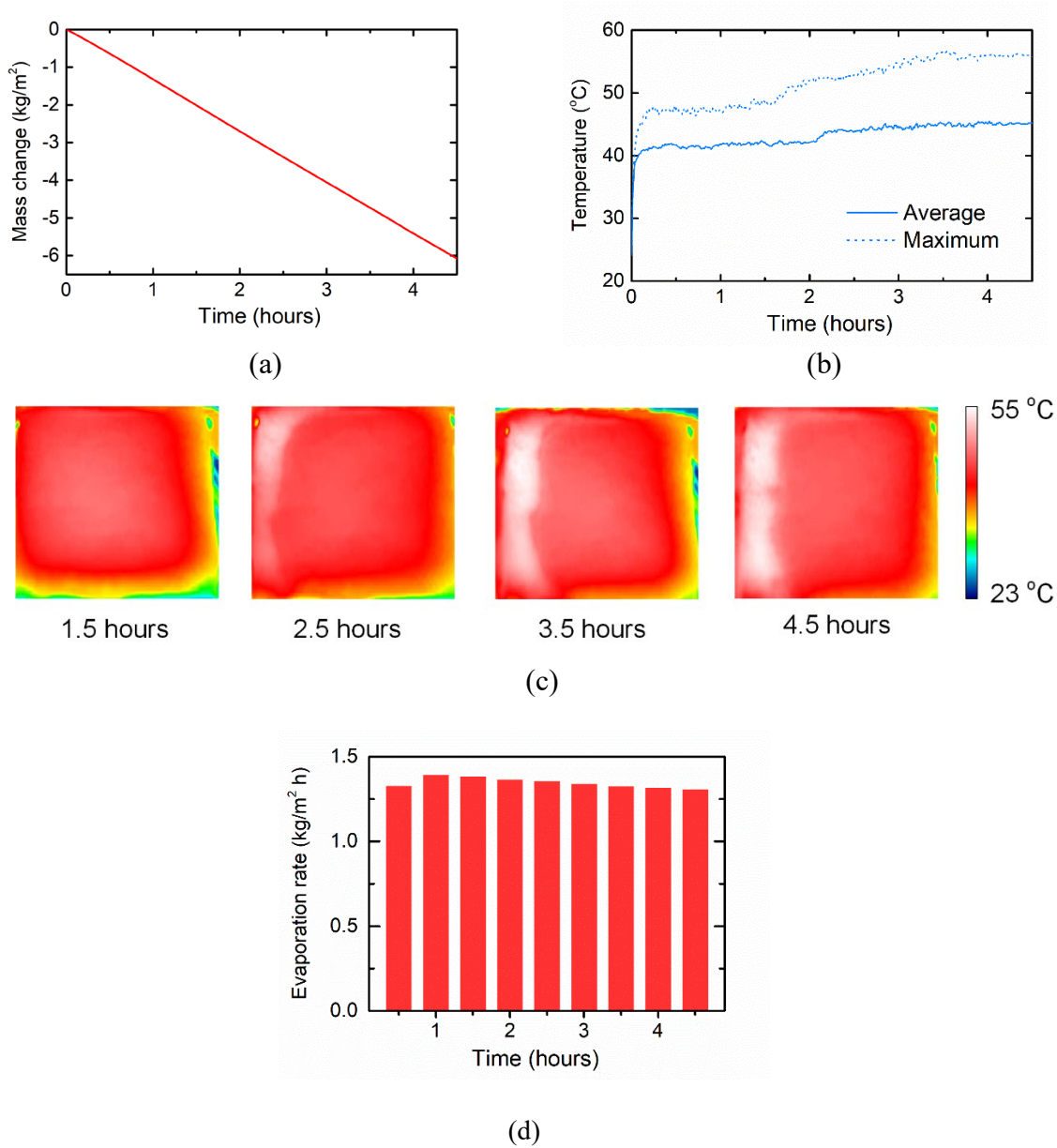


Fig. S13. Solar evaporation of 3.5 wt% NaCl solution with 2D evaporator design. (a) Mass change during the 4.5-hour evaporation test, showing an average evaporation rate of $1.35 \text{ kg m}^{-2} \text{ h}^{-1}$. (b) Average and maximum evaporator temperature during the 4.5-hour evaporation test. After the pre-heating stage, average temperature showed a slightly increase from $41 \text{ }^{\circ}\text{C}$ to $45 \text{ }^{\circ}\text{C}$, while the maximum temperature increased from $47 \text{ }^{\circ}\text{C}$ to $56 \text{ }^{\circ}\text{C}$. (c) IR images of the evaporator, showing stable and even temperature distribution during the evaporation. (d) The average evaporation rate in every half hour, showing continuous decrease after the preheating in the first hour.



Fig. S14. Experimental setup for the long-term Joule heating evaporation test. Two DC power sources were used to provide the same heating power, and the weight of two evaporation systems were measured at the same time. Such test could avoid the difference caused by the unstable ambient temperature and humidity.

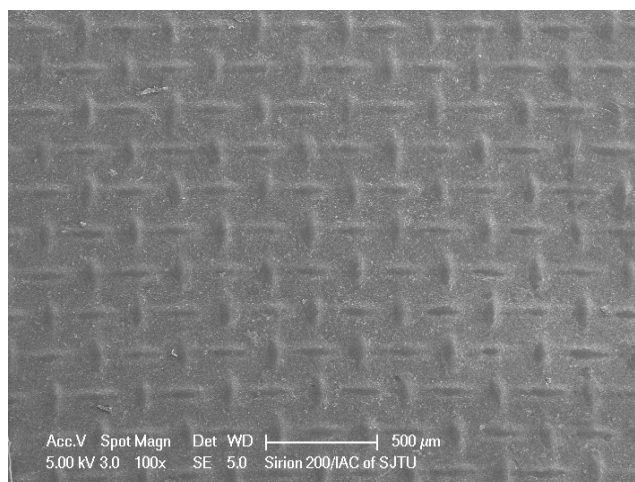


Fig. S15. SEM image of the membrane after evaporation test of CaSO₄ solution. No obvious contamination could be observed.

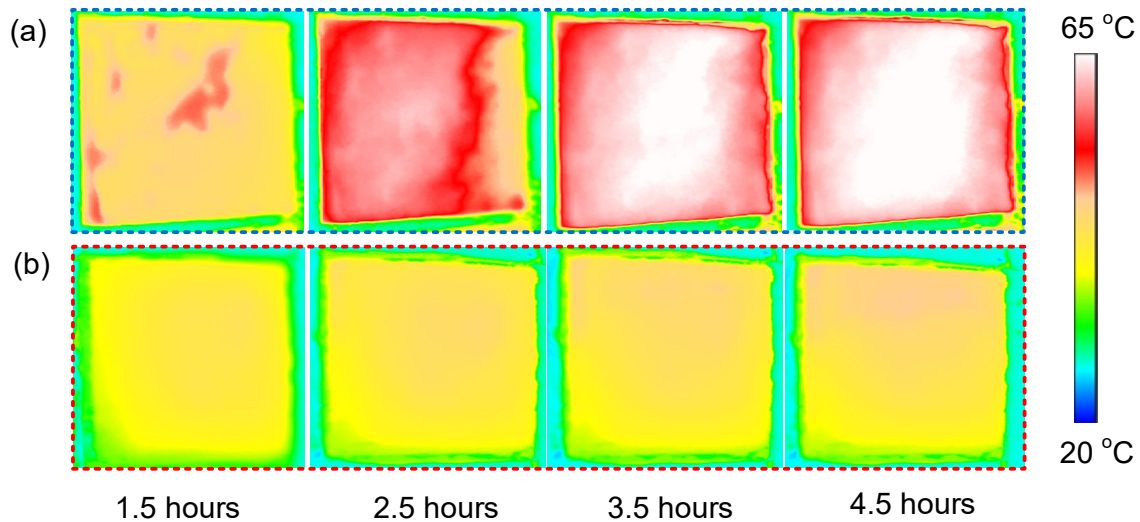


Fig. S16. Solar evaporation of compound solution with solute replacement and conventional designs. The compound solution contains 0.4 wt% NaAlg + 3.0 wt% NaCl + 1.0 wt% LiBr + saturated CaSO₄, and the evaporated solution contains 0.18 mol L⁻¹ NaCl and 0.18 mol L⁻¹ MgCl₂. (a) IR images of the solar evaporation without solute replacement. (b) IR images of the solar evaporation with solute replacement.

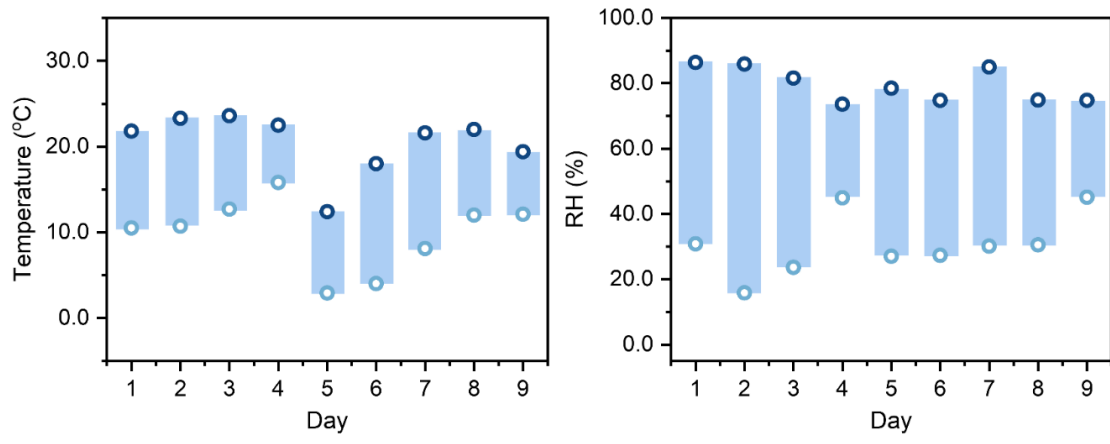
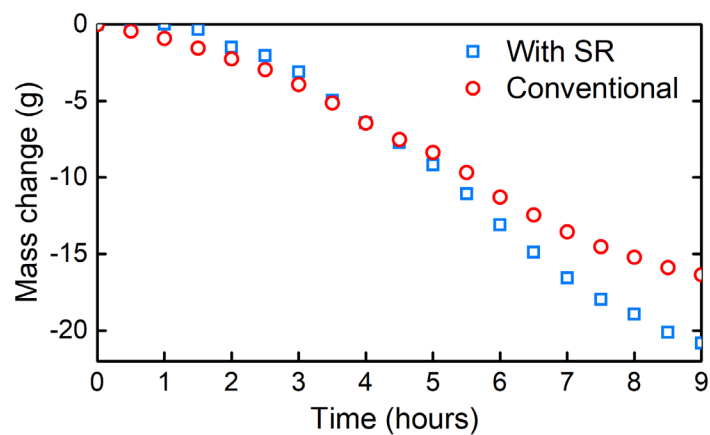
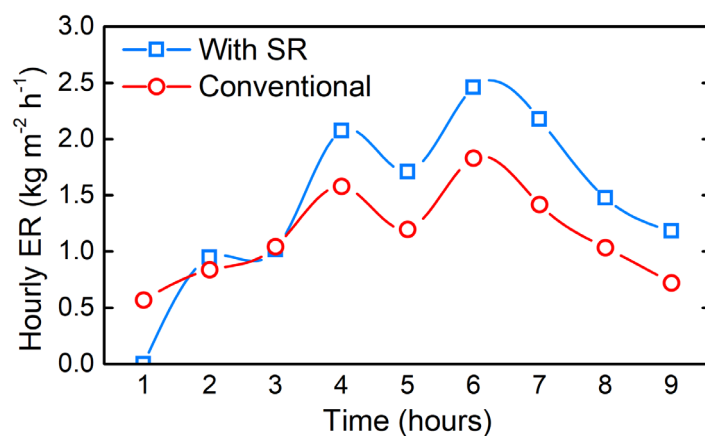


Fig. S17. The daily variations of ambient temperature, RHs during the outdoor tests.

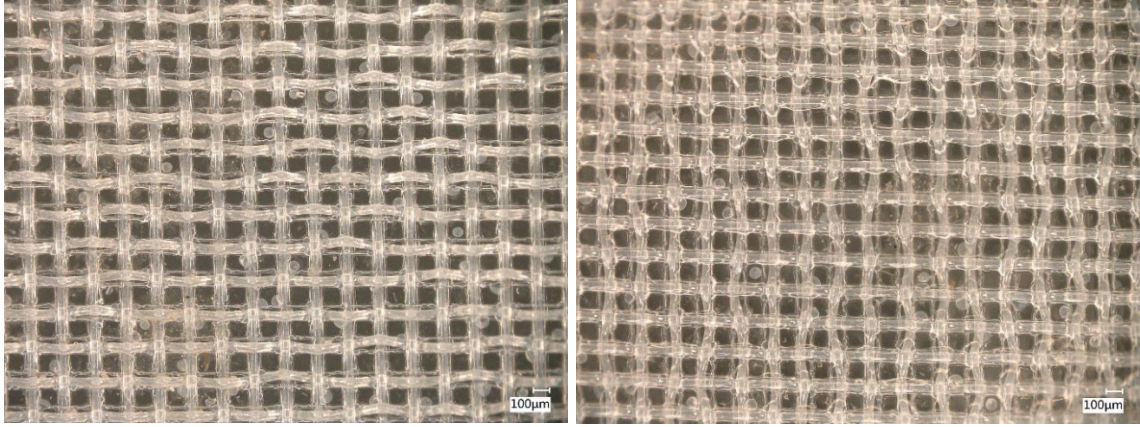


(a)



(b)

Fig. S18. Solar evaporation of compound solution under outdoor condition. (a) Mass change of compound solution on the second day. (b) Hourly evaporation rate on the second day. Highest hourly evaporation rate of $2.46 \text{ kg m}^{-2} \text{ h}^{-1}$ was obtained in the 6th hour.



(a)

(b)

Fig. S19. Microscopic images of the membrane after the outdoor evaporation test. (a) Images of membrane in contact with the treated solution. (b) Images of membrane in contact with the selected working fluid.

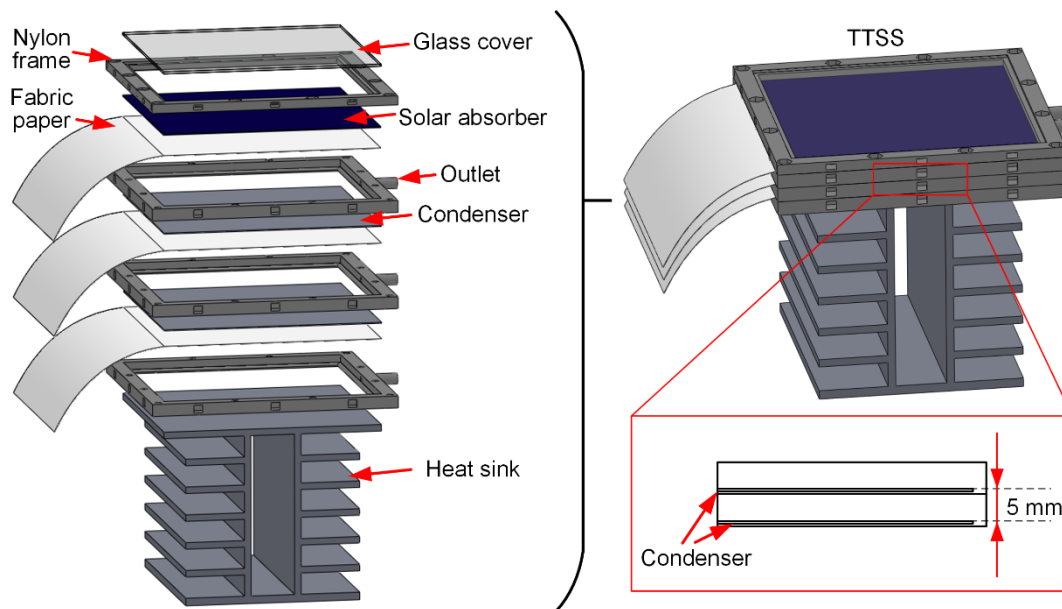


Fig. S20. Assembly of the thermally-localized multistage solar distiller. The first frame comprised a nylon frame, glass cover, solar absorber, and fabric paper as capillary wick. The middle frame comprised a nylon frame, condenser, and fabric paper. The last frame comprised a nylon frame and a heat sink as condenser. The frames were fastened with screw-nuts. The thickness of air gap in each stage was 5 mm.

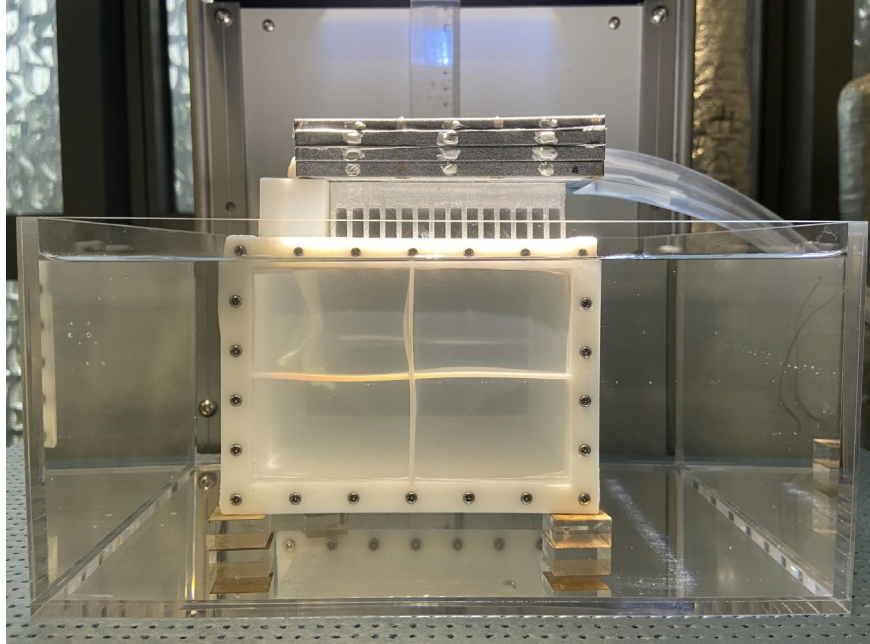


Fig. S21. The thermally-localized three-stage solar distiller with solute replacement.

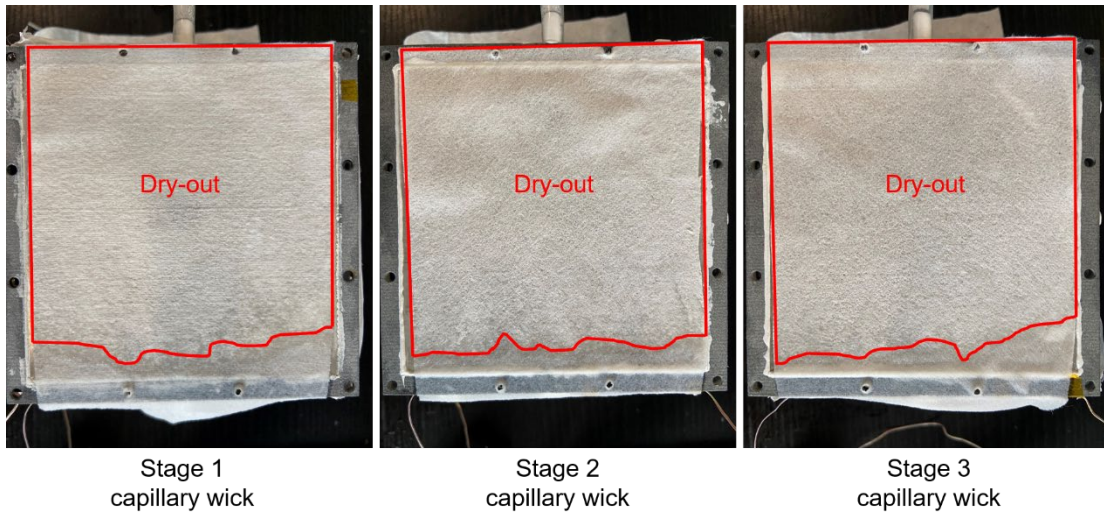


Fig. S22. The dry-out phenomenon on capillary evaporator of thermally localized multi-stage solar distillation without solute replacement. The almost fully dry-out regions on the capillary wicks were observed in every stage, as a result of the capillary pumping failure.

References

- [1] Ni G, Zandavi S H, Javid S M, et al. A salt-rejecting floating solar still for low-cost desalination. *Energy & Environmental Science*, 2018, 11(6): 1510-1519.
- [2] Zhang L, Xu Z, Bhatia B, et al. Modeling and performance analysis of high-efficiency thermally-localized multistage solar stills. *Applied Energy*, 2020, 266: 114864.
- [3] Luo X, Shi J, Zhao C, et al. The energy efficiency of interfacial solar desalination. *Applied Energy*, 2021, 302: 117581.
- [4] Wang L W, Metcalf S J, Critoph R E, et al. Development of thermal conductive consolidated activated carbon for adsorption refrigeration. *Carbon*, 2012, 50(3): 977-986.
- [5] Sharkh B A, Al-Amoudi A A, Farooque M, et al. Seawater desalination concentrate—a new frontier for sustainable mining of valuable minerals. *npj Clean Water*, 2022, 5(1): 9.
- [6] Harned H S, Hudson R M. The diffusion coefficient of magnesium sulfate in dilute aqueous solution at 25°. *Journal of the American Chemical Society*, 1951, 73(12): 5880-5882.
- [7] Le Gouellec Y A, Elimelech M. Control of calcium sulfate (gypsum) scale in nanofiltration of saline agricultural drainage water. *Environmental Engineering Science*, 2002, 19(6): 387-397.
- [8] Zhang C, Shi Y, Shi L, et al. Designing a next generation solar crystallizer for real seawater brine treatment with zero liquid discharge. *Nature Communications*, 2021, 12(1): 998.
- [9] Pérez-Calvo J F, Milella F, Ammann K, et al. Density and Viscosity of Aqueous (Ammonia+ Carbon Dioxide) Solutions at Atmospheric Pressure and Temperatures between 278.15 and 318.15 K. *Journal of Chemical & Engineering Data*, 2021, 66(4): 1787-1801.
- [10] Xu Z, Zhang L, Zhao L, Li B, Bhatia B, et al. Ultrahigh-efficiency desalination via a thermally-localized multistage solar still. *Energy & Environmental Science*, 2020, 13: 830-839.
- [11] Wang H, Gao Y, Gao B, et al. Comprehensive analysis of a hybrid FO-NF-RO process for seawater desalination: With an NF-like FO membrane. *Desalination*, 2021, 515: 115203.